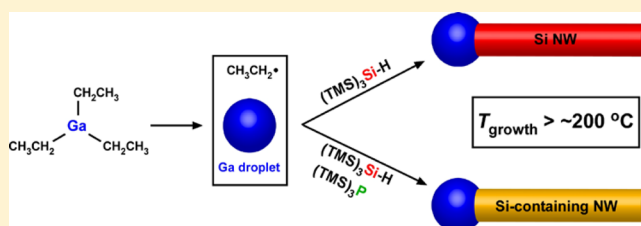


# Low-Temperature Solution-Phase Growth of Silicon and Silicon-Containing Alloy Nanowires

Jianwei Sun,<sup>†,‡,⊥</sup> Fan Cui,<sup>†,‡,⊥</sup> Christian Kisielowski,<sup>§,||</sup> Yi Yu,<sup>†</sup> Nikolay Kornienko,<sup>†</sup> and Peidong Yang<sup>\*,†,‡</sup><sup>†</sup>Department of Chemistry, University of California, Berkeley, California 94720, United States<sup>‡</sup>Materials Science Division, <sup>§</sup>National Center for Electron Microscopy, and <sup>||</sup>Joint Center for Artificial Photosynthesis (JCAP), Lawrence Berkeley National Laboratory, Berkeley, California 94720, United States**S** Supporting Information

**ABSTRACT:** Low-temperature synthesis of crystalline silicon and silicon-containing nanowires remains a challenge in synthetic chemistry due to the lack of sufficiently reactive Si precursors. We report that colloidal Si nanowires can be grown using tris(trimethylsilyl)silane or trisilane as the Si precursor by a Ga-mediated solution–liquid–solid (SLS) approach at temperatures of about 200 °C, which is more than 200 °C lower than that reported in the previous literature. We further demonstrate that the new Si chemistry can be adopted to incorporate Si atoms into III–V semiconductor lattices, which holds promise to produce a new Si-containing alloy semiconductor nanowire. This development represents an important step toward low-temperature fabrication of Si nanowire-based devices for broad applications.



## 1. INTRODUCTION

Silicon (Si) is the most important semiconductor in the microelectronics industry. Continuous device miniaturization has led to the emergence of the nanoelectronics industry, in which Si nanowires (NWs) can play an essential role. For example, proof-of-principle Si-NW-based electronic nano-devices have been demonstrated.<sup>1</sup> In the photovoltaics industry, crystalline Si modules are the most frequently used and heavily studied material. Device physics modeling has suggested that radial p–n junction NW photovoltaic devices can potentially achieve higher efficiency relative to the conventional planar devices because the unique one-dimensional structure allows both good light absorption and efficient charge carrier collection.<sup>2</sup> This device concept has been demonstrated at both a single NW level and oriented NW array level.<sup>3,4</sup> In addition, Si NW array-based energy conversion devices such as solar water-splitting cells and lithium-ion batteries have also been reported recently.<sup>5,6</sup>

To date, the Si NW-based devices have been predominantly fabricated by either top-down methods using single-crystalline Si wafers or bottom-up methods using metal nanoparticles (NPs) and molecular Si precursors via a vapor–liquid–solid (VLS) mechanism.<sup>7</sup> Compared to the top-down methods, the bottom-up methods offer greater flexibility in controlling NW properties but generally require high growth temperatures even for the metals that can form eutectic phase at low temperature with Si. To achieve low-temperature (<400 °C) VLS growth of Si NWs, the Si precursors must be activated (or dissociated) first. This can be achieved by means of in situ H<sub>2</sub> plasma treatment, which has resulted in the growth of Si NWs at temperatures as low as 240 °C.<sup>8</sup>

Semiconductor NW growth can also be achieved in solution via a solution–liquid–solid (SLS) mechanism using metal NPs with low melting points.<sup>9</sup> Compared to the VLS method, the SLS method has the advantage of surface passivation, ease of implementation, and large-scale production.<sup>10</sup> As such, the SLS approach is potentially promising for cost-effective solution-processable fabrication of NW-based devices. Recently, metal NP-mediated SLS growth of Si NWs or nanorods has been reported.<sup>11–13</sup> However, the growth temperatures are mostly higher than 410 °C because the precursor activation method employed in the VLS growth cannot be directly adopted in the solution-phase synthesis. Very recently, it was reported that short Si nanorods (<50 nm in length) could be grown by a Sn-seeded SLS method using cyclohexasilane as the Si precursor at temperatures as low as 200 °C.<sup>14</sup> In general, it remains a big challenge in the SLS chemistry to achieve Si NW growth at low temperatures.

Herein we report that both tris(trimethylsilyl)silane [(TMS)<sub>3</sub>SiH], which is widely used as a radical-based reducing agent in organic synthesis,<sup>15</sup> and trisilane can be used as the Si precursor for Ga-catalyzed SLS growth of colloidal Si NWs at temperatures of about 200 °C, which is more than 200 °C lower than the previously reported SLS growth temperatures and also lower than that achieved in the VLS growth. In addition, we demonstrate that Si atoms can be incorporated

**Special Issue:** Richard P. Van Duyne Festschrift**Received:** August 25, 2015**Revised:** November 13, 2015**Published:** November 30, 2015

into III–V semiconductor NW lattices, which holds great promise to grow new alloy semiconductor NWs with tunable properties.

## 2. RESULTS AND DISCUSSION

Ga was chosen as our SLS catalyst for two reasons. First, the Ga–Si system has a very low eutectic temperature of 30 °C (Supporting Information, Figure S1), which is ideal for low-temperature growth of Si NWs. Second, Ga NPs are readily accessible through thermal decomposition of organometallic Ga precursors.<sup>16</sup> Our synthesis was conducted in a noncoordinating saturated hydrocarbon solvent such as hexadecane and squalane. No surfactants were added. In a typical synthesis, a mixed precursor solution containing 0.15 mmol of triethylgallium (TEG) and 1 mmol of  $(\text{TMS})_3\text{SiH}$  in 2 g of hexadecane was quickly injected into a preheated hexadecane (15 g) under vigorous magnetic stirring at a certain temperature in the range of 200–300 °C. The reaction mixture remained clear for a short period of time and then turned to yellowish, indicating formation of Ga NPs. After this, the solution gradually changed to dark brown, indicating NW growth.

The transmission electron microscopy (TEM) image of an as-grown sample prepared at 274 °C shows NWs with attached NPs at one end (Figure 1a). We note that some NPs are

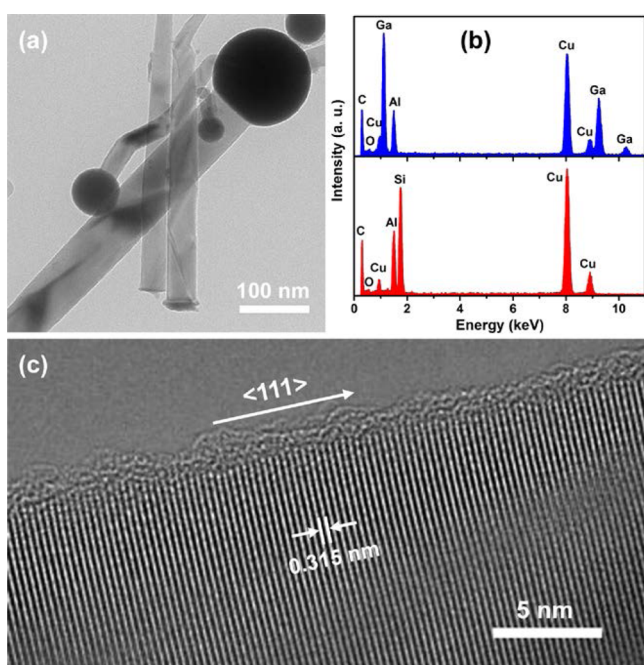


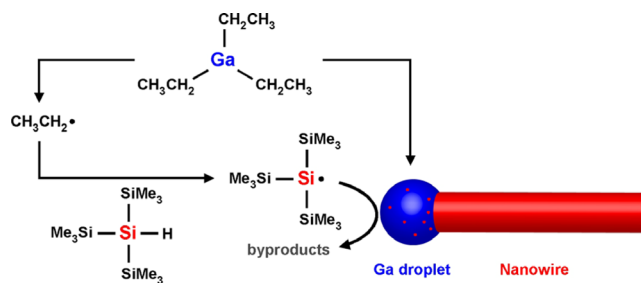
**Figure 1.** (a) TEM image of an as-grown sample synthesized using triethylgallium and tris(trimethylsilyl)silane precursors in hexadecane at 274 °C, showing nanowires with attached nanoparticles at one end. (b) EDS spectra collected from the nanoparticle (top panel, in blue) and the nanowire (bottom panel, in red). The Cu and C signals are from the Cu TEM grids with C support. The Al signals are from the Al sample holder. (c) HRTEM image of a single nanowire.

detached from the wires, which is likely due to the ultrasonication step in the NW purification process for preparing TEM samples. Energy-dispersive X-ray spectra (EDS) collected from the NP and the NW show Ga and Si signals, respectively, confirming the Ga-catalyzed SLS growth of Si NWs (Figure 1b). No Si was detected in the NP, which is consistent with the very low solubility of Si in Ga (Figure S1).

The weak oxygen peaks in the EDS spectra suggest that both the Ga NPs and the Si NWs are surface oxidized. The expected diamond cubic crystal structure of the Si NWs was confirmed by powder X-ray diffraction (XRD, see Figure S2 in the Supporting Information). The high-resolution TEM (HRTEM) image of a single NW (Figure 1c) shows the single-crystalline nature of the wires. The spacing of the well-resolved lattice fringes perpendicular to the NW growth direction was measured to be 0.315 nm, which is consistent with the  $d$  spacing of the (111) planes in cubic Si and indicates the  $\langle 111 \rangle$  wire growth direction. The amorphous layer on the nanowire surface is composed of oxidized silicon and surface-adsorbed organic molecules.

To find out the lower limit for the NW growth, we further decreased the reaction temperature. Interestingly, we observed NW growth at a temperature as low as 210 °C (Supporting Information, Figure S3).

### Scheme 1. Proposed Free-Radical Involved Solution–Liquid–Solid (SLS) Growth of Colloidal Si Nanowires Using Triethylgallium and Tris(trimethylsilyl)silane as the Precursors at Low Temperatures



To understand the dramatic growth temperature decrease of Ga-catalyzed Si NWs, a control experiment was conducted in the absence of TEG but showed no silicon nanowire growth, indicating that TEG plays a critical role in catalyzing the reaction. The role of TEG can be 2-fold. First, thermal decomposition of TEG produces nanoscale gallium metal particles in the solution, which were observed in the TEM study. As proposed in many SLS mechanism studies,<sup>10,15</sup> melted metal droplets can provide ideal surfaces, lowering the energy barrier for precursor absorption and decomposition. This could be the main reason that accounts for the sharply decreased reaction temperature. Second, it is well-known that thermal decomposition of TEG not only produces Ga metal but also releases ethyl radicals.<sup>17</sup> The active radical species could help break the Si–Si or Si–H bond in the precursor as analogous to the Si precursor activation pathway using  $\text{H}_2$  plasma treatment for the low-temperature gas-phase Si NW growth. Particularly in the case of using  $(\text{TMS})_3\text{SiH}$  as the Si source, the alkyl radical can react with  $(\text{TMS})_3\text{SiH}$  to generate  $(\text{TMS})_3\text{Si}\cdot$  radicals. We believe that  $(\text{TMS})_3\text{Si}\cdot$  radicals serve as the active species for silicon growth and that the ethyl-free radical accelerated the production of silyl radicals.<sup>18,19</sup> Other control experiments in replacement of  $(\text{TMS})_3\text{SiH}$  with organosilanes that have similar molecular structures but are more difficult to form free radicals, including  $[(\text{TMS})_3\text{SiCl}]$  and tetrakis(trimethylsilyl)silane  $[(\text{TMS})_4\text{Si}]$ , failed to grow Si NWs, which further supports our proposed reaction pathway.

Recently, Si-containing IV–III–V semiconductor films have been synthesized at high temperatures ( $\sim 500$  °C) by a gas-phase molecular beam epitaxy (MBE) method.<sup>20–22</sup> Another

work demonstrated that Si can be used as dopants in III–V materials.<sup>23</sup> Theoretical calculations have shown that these materials would be promising for solar energy conversion due to significantly enhanced visible-light absorption relative to Si.<sup>24</sup> Because of our success in the Si NW growth discussed above, we next investigated the possibility of using  $(\text{TMS})_3\text{SiH}$  to incorporate Si atoms into other semiconductor lattices to produce new silicon-containing alloy NWs in a solution-phase synthesis at low temperatures. Owing to our previous success in self-seeded SLS growth of GaP NWs,<sup>16</sup> we naturally combined the Si and GaP syntheses at the same growth conditions (shown below).

Figure 2a and b show the low- and high-magnification bright-field TEM images of Ga-removed GaP NWs synthesized using TEG and tris(trimethylsilyl)phosphine  $[(\text{TMS})_3\text{P}]$  precursors in hexadecane at 278 °C. The wires are typically longer than 1  $\mu\text{m}$  and have relatively uniform diameter along the length of the wire. When we introduced an increasing amount of  $(\text{TMS})_3\text{SiH}$

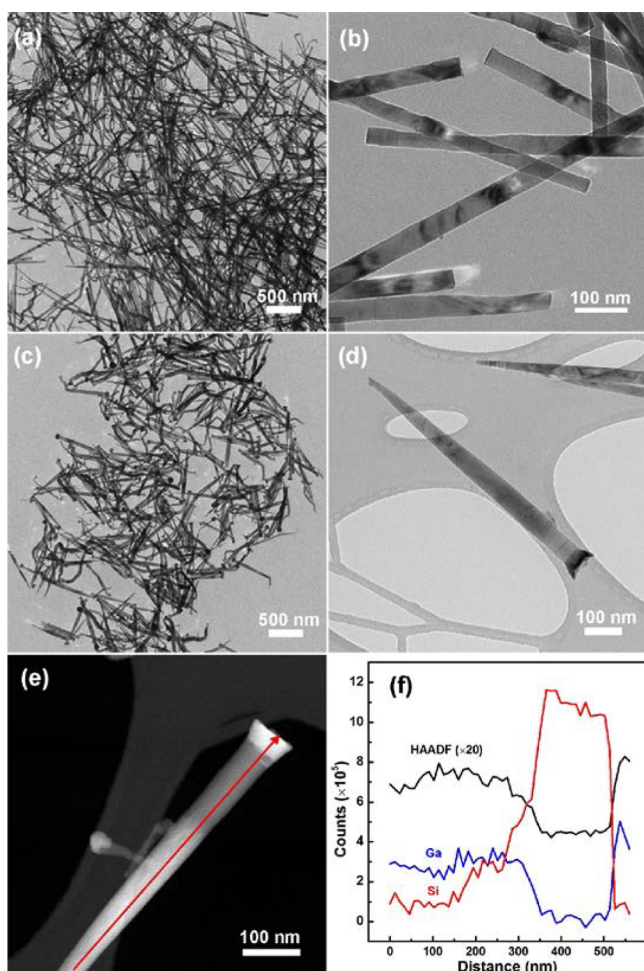


**Figure 2.** (a) and (b) Low- and high-magnification TEM images of Ga-removed GaP nanowires synthesized using TEG and  $(\text{TMS})_3\text{P}$  precursors in hexadecane at 278 °C. (c) and (d) Low- and high-magnification TEM images of Ga-removed Si–GaP mixture nanowires synthesized using TEG,  $(\text{TMS})_3\text{P}$ , and  $(\text{TMS})_3\text{SiH}$  precursors in hexadecane at 277 °C. The initial Si:GaP ratio was 1:1. (e) High-angle annular dark field (HAADF) image of a single Si–GaP mixture nanowire. The red arrow shows an EELS line scan pathway. (f) The intensity of HAADF, Ga, and Si signals vs distance along the line scan pathway shown in (e).

into the GaP growth solution, the obtained wires became shorter and more tapered and frequently exhibited diameter expansion at the larger-diameter end (Figure 2c and d), indicating that the growth behavior of the new wires is quite different from that of GaP. A high-angle annular dark field (HAADF) image of a single wire (Figure 2e) exhibits substantial Z-contrast along the growth direction because of the largely different atomic numbers of Si ( $Z = 14$ ) and Ga ( $Z = 31$ ).<sup>25</sup> Electron energy loss spectra (EELS) were collected along the wire length from a point near the small-diameter end (corresponding to the initial growth) all the way to the large-diameter end (corresponding to the final growth). They reveal the presence of four distinct growth stages (Figure 2f). During the initial wire growth for  $\sim 150$  nm, GaP dominated. Then, an increasing amount of Si was incorporated into the wire for a distance of  $\sim 200$  nm, forming a  $\text{Si}_x(\text{GaP})_y$  region. Si dominated at the third stage. Finally, GaP dominated again, which is likely due to the complete consumption of the in situ generated  $(\text{TMS})_3\text{Si}\bullet$  radicals or the further GaP growth during the cooling process. This inhomogeneous distribution of elements along the length of the nanowire suggested unbalanced reactivities of the molecular precursors during the nanowire growth. Although further efforts are needed to fully understand this complex NW growth behavior, our results have already demonstrated the possibility of incorporating Si into other semiconductor lattices at low temperatures.

An interesting question regarding the  $\text{Si}_x(\text{GaP})_y$  region in the NW is whether the element distributions are atomically homogeneous or not. To address this question, we next used a TEAM 0.5 microscope, which is a double-aberration-corrected transmission electron microscope capable of producing images with 50 pm resolution,<sup>26</sup> to acquire an atomically resolved Z-contrast image of the  $\text{Si}_x(\text{GaP})_y$  region in the  $\langle 110 \rangle$  projection (Figure 3a). This allowed us to identify composition fluctuations locally by detecting the asymmetrical GaP dumbbells and the symmetrical Si dumbbells (Figure 3b–d). The image shows that GaP- and Si-rich nanometer-sized domains exist, indicating compositional inhomogeneity in the  $\text{Si}_x(\text{GaP})_y$  region, while the crystal structure of each component is maintained. This implies that lattice mismatched growth occurred since the lattice parameters of Si ( $a = 0.543$  nm) differ from the ones of GaP ( $a = 0.545$  nm). Interestingly, we frequently observed the transition from the Ga–P dumbbells to the P–Ga dumbbells separated by Si–Si dumbbells, indicating the polarity reversal of GaP across the Si-rich region (Figure 3b), which can significantly alter the properties of the materials.<sup>27</sup>

On the basis of the clear evidence of nanoscale mixing of GaP and Si, an intriguing tunable property one may expect is the tunable bandgap. Using 80 kV monochromated valence EELS (VEELS)<sup>28–30</sup> measurements by the TEAM 1 microscope, we successfully measured the bandgap change along a single NW (Figure 4). Monochromated VEELS provides high spatial resolution while maintaining good energy resolution ( $\sim 100$  meV) (Figure S4), offering the opportunity of detecting bandgap changes on the tens of nanometer level. For the bandgap measurement (Figure S4), the influence of zero-loss peak was removed using a power-law subtraction,<sup>31,32</sup> and the bandgap values were obtained by fitting the intensity onset with  $(E - E_g)^{3/2}$  type function as both GaP and Si are indirect bandgaps.<sup>29,33,34</sup> As shown in Figure 4, the bandgap values approach to the theoretical 2.3 eV of GaP at the two ends of GaP-dominated regions, whereas in the mixture region, the

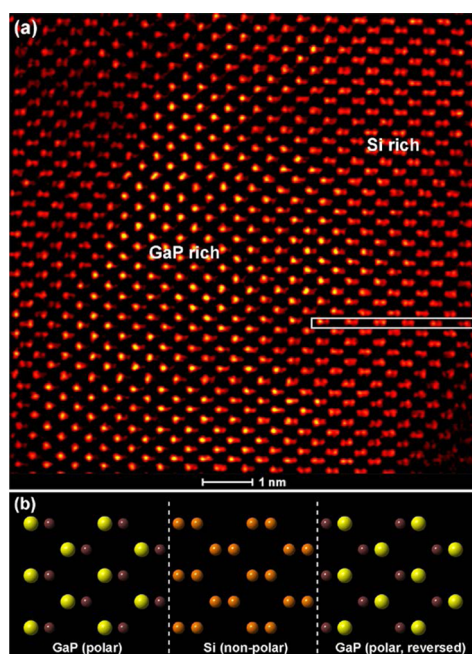


**Figure 3.** (a) Atomically resolved Z-contrast image acquired from the  $\text{Si}_x(\text{GaP})_y$  region in the  $\langle 110 \rangle$  projection. The asymmetrical GaP and symmetrical Si dumbbells can be seen in this projection. The white box highlights a transition from the Ga–P dumbbell to the P–Ga dumbbell separated by Si–Si dumbbells. (b) Structural model of the polarity reversal of the GaP lattice induced by the nonpolar Si lattice.

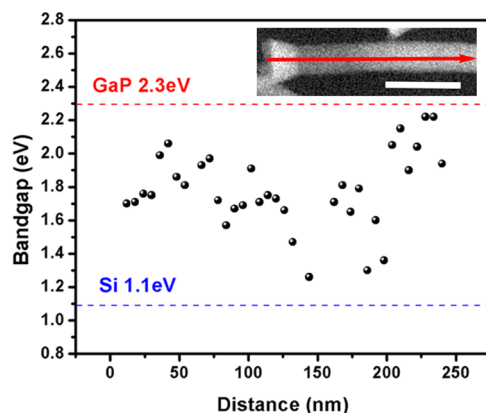


**Figure 4.** Bandgap values vs distance along the line scan through a single NW. Inset is the corresponding HAADF image. Scale bar, 100 nm.

bandgaps tend to decrease to the level of Si (1.1 eV). The probable reason that the edge bandgap only approaches but is not equal to 2.3 eV is that the GaP-dominated region at the end of the wire is not purely GaP. They still have sparse silicon atoms distributed within the lattice. The fluctuation of some data points may be attributed to the random distribution of GaP- and Si-rich domains in the mixture region, which also confirms our previous conclusion of the compositional inhomogeneity.

To further balance the precursor reactivities in order to achieve homogeneous growth of Si-containing alloy nanowires, we replaced  $(\text{TMS})_3\text{SiH}$  with trisilane ( $\text{Si}_3\text{H}_8$ ), which is a highly pyrophoric Si precursor with higher reactivity. Different from the relatively short tapered wires (Figure 2d), less-tapered long wires were obtained by using TEG,  $(\text{TMS})_3\text{P}$ , and  $\text{Si}_3\text{H}_8$

precursors at a lower temperature of 180 °C (Figure S5). EDS analysis along the length of individual nanowires showed much more homogeneous Si distribution (Figure S6), indicating that the reactivities of the three precursors were better balanced. However, HRTEM images still showed GaP- and Si-rich nanometer-sized domains. Further efforts such as using single-source precursors are necessary to achieve growth of new Si-containing alloy nanowires with atomically homogeneous composition.

### 3. CONCLUSION

In summary, we have shown that both  $(\text{TMS})_3\text{SiH}$ , a free radical-based reducing agent in organic synthesis, and  $\text{Si}_3\text{H}_8$  are sufficiently reactive Si precursors for the Ga-catalyzed SLS growth of colloidal Si NWs at record low temperatures. Unlike Au, which is the most widely used catalyst material for the growth of Si NWs but is known to be deleterious to the electronic properties of Si, Ga is a shallow p-type acceptor and will not introduce trap sites that serve as the undesired electron–hole recombination centers.<sup>35</sup> Therefore, our low-temperature Ga-catalyzed synthesis holds great promise for cost-effective solution-processable fabrication of Si NW-based devices that would find applications in broad fields such as electronics and energy conversions. In addition, we also demonstrated the possibility of incorporating Si atoms into III–V semiconductor NWs at low temperatures, which could open new avenues for growing novel alloy semiconductor NWs with tunable properties.

### ■ ASSOCIATED CONTENT

#### Supporting Information

The Supporting Information is available free of charge on the ACS Publications website at DOI: 10.1021/acs.jpcc.5b08289.

Additional phase diagram, XRD data, and TEM/EELS/EDS data (PDF)

### ■ AUTHOR INFORMATION

#### Corresponding Author

\*E-mail: p\_yang@berkeley.edu.

#### Author Contributions

<sup>†</sup>These authors contributed equally to this work.

#### Notes

The authors declare no competing financial interest.

### ■ ACKNOWLEDGMENTS

This work (including the work performed at NCEM) is supported by the Office of Science, Office of Basic Energy Sciences of the U.S. Department of Energy under Contract No. DE-AC02–05CH11231 (PChem). We thank Peter Ercius and Chengyu Song for helpful discussion and assistance of TEAM 1 experiment. The microscopy work by CK is performed by the Joint Center for Artificial Photosynthesis, a DOE Energy Innovation Hub, supported through the Office of Science of the U.S. Department of Energy under Award Number DE-SC0004993.

### ■ REFERENCES

- (1) Cui, Y.; Lieber, C. M. Functional Nanoscale Electronic Devices Assembled Using Silicon Nanowire Building Blocks. *Science* **2001**, *291*, 851–853.

- (2) Kayes, B. M.; Atwater, H. A.; Lewis, N. S. Comparison of the Device Physics Principles of Planar and Radial P–N Junction Nanorod Solar Cells. *J. Appl. Phys.* **2005**, *97*, 114302–114311.
- (3) Tian, B.; Zheng, X.; Kempa, T. J.; Fang, Y.; Yu, N.; Yu, G.; Huang, J.; Lieber, C. M. Coaxial Silicon Nanowires as Solar Cells and Nanoelectronic Power Sources. *Nature* **2007**, *449*, 885–889.
- (4) Garnett, E. C.; Yang, P. Silicon Nanowire Radial p–n Junction Solar Cells. *J. Am. Chem. Soc.* **2008**, *130*, 9224–9225.
- (5) Liu, C.; Tang, J.; Chen, H.; Liu, B.; Yang, P. A Fully Integrated Nanosystem of Semiconductor Nanowires for Direct Solar Water Splitting. *Nano Lett.* **2013**, *13*, 2989–93.
- (6) Chan, C. K.; Peng, H.; Liu, G.; McIlwrath, K.; Zhang, X. F.; Huggins, R. A.; Cui, Y. High-performance Lithium Battery Anodes Using Silicon Nanowires. *Nat. Nanotechnol.* **2008**, *3*, 31–35.
- (7) Dasgupta, N. P.; Sun, J.; Liu, C.; Brittan, S.; Andrews, S. C.; Lim, J.; Gao, H.; Yan, R.; Yang, R. 25th Anniversary Article: Semiconductor Nanowires – Synthesis, Characterization, and Applications. *Adv. Mater.* **2014**, *26*, 2137–56.
- (8) Yu, L.; O'Donnell, B.; Alet, P.-J.; Conesa-Boj, S.; Peiró, F.; Arbiol, J.; Cabarrocas, P. R. I. Plasma-Enhanced Low Temperature Growth of Silicon Nanowires and Hierarchical Structures by Using Tin and Indium Catalysts. *Nanotechnology* **2009**, *20*, 225604.
- (9) Trentler, T. J.; Hickman, K. M.; Goel, S. C.; Viano, A. M.; Gibbons, P. C.; Buhro, W. E. Solution-Liquid-Solid Growth of Crystalline III-V Semiconductors: An Analogy to Vapor-Liquid-Solid Growth. *Science* **1995**, *270*, 1791–1794.
- (10) Wang, F.; Dong, A.; Sun, J.; Tang, R.; Yu, H.; Buhro, W. E. Solution–Liquid–Solid Growth of Semiconductor Nanowires. *Inorg. Chem.* **2006**, *45*, 7511–7521.
- (11) Heitsch, A. T.; Fanfair, D. D.; Tuan, H.-Y.; Korgel, B. A. Solution–Liquid–Solid (SLS) Growth of Silicon Nanowires. *J. Am. Chem. Soc.* **2008**, *130*, 5436–5437.
- (12) Heitsch, A. T.; Hessel, C. M.; Akhavan, V. A.; Korgel, B. A. Colloidal Silicon Nanorod Synthesis. *Nano Lett.* **2009**, *9*, 3042–3047.
- (13) Lu, X.; Hessel, C. M.; Yu, Y.; Bogart, T. D.; Korgel, B. A. Colloidal Luminescent Silicon Nanorods. *Nano Lett.* **2013**, *13*, 3101–3105.
- (14) Lu, X.; Anderson, K. J.; Boudjouk, P.; Korgel, B. A. Low Temperature Colloidal Synthesis of Silicon Nanorods from Isotetrasilane, Neopentasilane, and Cyclohexasilane. *Chem. Mater.* **2015**, *27*, 6053–6058.
- (15) Chatgililoglu, C. (Me<sub>3</sub>Si)<sub>3</sub>SiH: Twenty Years After Its Discovery as a Radical-Based Reducing Agent. *Chem. - Eur. J.* **2008**, *14*, 2310–2320.
- (16) Sun, J.; Liu, C.; Yang, P. Surfactant-Free, Large-Scale, Solution–Liquid–Solid Growth of Gallium Phosphide Nanowires and Their Use for Visible-Light-Driven Hydrogen Production from Water Reduction. *J. Am. Chem. Soc.* **2011**, *133*, 19306–19309.
- (17) Williams, J. O.; Hoare, R. D.; Khan, O.; Parrott, M. J.; Cole-Hamilton, D. J.; Griffiths, R. J. M. Mechanisms in Metal–Organic Chemical Vapour Deposition [and Discussion]. *Philos. Trans. R. Soc., A* **1990**, *330*, 183–193.
- (18) Chatgililoglu, C. Organosilanes as Radical-Based Reducing Agents in Synthesis. *Acc. Chem. Res.* **1992**, *25*, 188–194.
- (19) Chatgililoglu, C.; Griller, D.; Lesage, M. Research Article Prev. Article Next Article Table of Contents Tris(trimethylsilyl)silane. A New reducing Agent. *J. Org. Chem.* **1988**, *53*, 3641–3642.
- (20) Watkins, T.; Chizmeshya, A. V. G.; Jiang, L.; Smith, D. J.; Beeler, R. T.; Grzybowski, G.; Poweleit, C. D.; Menéndez, J.; Kouvetakis, J. Nanosynthesis Routes to New Tetrahedral Crystalline Solids: Silicon-like Si<sub>3</sub>AlP. *J. Am. Chem. Soc.* **2011**, *133*, 16212–16218.
- (21) Grzybowski, G.; Watkins, T.; Beeler, R. T.; Jiang, L.; Smith, D. J.; Chizmeshya, A. V. G.; Kouvetakis, J.; Menéndez, J. Synthesis and Properties of Monocrystalline Al(As<sub>1-x</sub>P<sub>x</sub>)Si<sub>3</sub> Alloys on Si(100). *Chem. Mater.* **2012**, *24*, 2347–2355.
- (22) Kouvetakis, J.; Chizmeshya, A. V. G.; Jiang, L.; Watkins, T.; Grzybowski, G.; Beeler, R. T.; Poweleit, C.; Menéndez, J. Monocrystalline Al(As<sub>1-x</sub>N<sub>x</sub>)Si<sub>3</sub> and Al(P<sub>1-x</sub>N<sub>x</sub>)<sub>y</sub>Si<sub>5-2y</sub> Alloys with Diamond-like Structures: New Chemical Approaches to Semiconductors Lattice Matched to Si. *Chem. Mater.* **2012**, *24*, 3219–3230.
- (23) Fang, Z.; Robin, E.; Rozas-Jiménez, E.; Cros, A.; Donatini, F.; Mollard, N.; Pernot, J.; Daudin, B. Si Donor Incorporation in GaN Nanowires. *Nano Lett.* **2015**, *15*, 6794–6801.
- (24) Yang, J.-H.; Zhai, Y.; Liu, H.; Xiang, H.; Gong, X.; Wei, S.-H. Si<sub>3</sub>AlP: A New Promising Material for Solar Cell Absorber. *J. Am. Chem. Soc.* **2012**, *134*, 12653–12657.
- (25) Pennycook, S. J. Z-Contrast Transmission Electron Microscopy: Direct Atomic Imaging of Materials. *Annu. Rev. Mater. Sci.* **1992**, *22*, 171–195.
- (26) Kisielowski, C.; Freitag, B.; Bischoff, M.; van Lin, H.; Lazar, S.; Knippels, G.; Tiemeijer, P.; van der Stam, M.; von Harrach, S.; Stekelenburg, M.; et al. Detection of Single Atoms and Buried Defects in Three Dimensions by Aberration-Corrected Electron Microscope with 0.5-Å Information Limit. *Microsc. Microanal.* **2008**, *14*, 469–477.
- (27) Cohen, D.; McKernan, S.; Carter, C. B. Characterization of the Absolute Crystal Polarity Across Twin Boundaries in Gallium Phosphide Using Convergent-Beam Electron Diffraction. *Microsc. Microanal.* **1999**, *5*, 173–186.
- (28) Kimoto, K.; Kothleitner, G.; Grogger, W.; Matsui, Y.; Hofer, F. Advantages of a Monochromator for Bandgap Measurements Using Electron Energy-loss Spectroscopy. *Micron* **2005**, *36*, 185–189.
- (29) Erni, R.; Browning, N. D. Valence Electron Energy-Loss Spectroscopy in Monochromated Scanning Transmission Electron Microscopy. *Ultramicroscopy* **2005**, *104*, 176–192.
- (30) Stöger-Pollach, M. Optical Properties and Bandgaps from Low Loss EELS: Pitfalls and Solutions. *Micron* **2008**, *39*, 1092–1110.
- (31) Specht, P.; Ho, J. C.; Xu, X.; Armitage, R.; Weber, E. R.; Erni, R.; Kisielowski, C. Band Transitions in Wurtzite GaN and InN Determined by Valence Electron Energy Loss Spectroscopy. *Solid State Commun.* **2005**, *135*, 340–344.
- (32) Erni, R.; Browning, N. D. Quantification of the Size-Dependent Energy Gap of Individual CdSe Quantum Dots by Valence Electron Energy-Loss Spectroscopy. *Ultramicroscopy* **2007**, *107*, 267–273.
- (33) Rafferty, B.; Brown, L. Direct and Indirect Transitions in the Region of the Band Gap Using Electron-Energy-Loss Spectroscopy. *M. Phys. Rev. B: Condens. Matter Mater. Phys.* **1998**, *58*, 10326–10337.
- (34) Lazar, S.; Botton, G. A.; Wu, M.-Y.; Tichelaar, F. D.; Zandbergen, H. W. Materials Science Applications of HREELS in Near Edge Structure Analysis and Low-Energy Loss Spectroscopy. *Ultramicroscopy* **2003**, *96*, 535–546.
- (35) Schmidt, V.; Wittemann, J. V.; Gösele, U. Growth, Thermodynamics, and Electrical Properties of Silicon Nanowires. *Chem. Rev.* **2010**, *110*, 361–388.